Bioactive Materials 34 (2024) 338–353

Contents lists available at ScienceDirect

Bioactive Materials

journal homepage: www.keaipublishing.com/en/journals/bioactive-materials

# Integrating coaxial electrospinning and 3D printing technologies for the development of biphasic porous scaffolds enabling spatiotemporal control in tumor ablation and osteochondral regeneration

Wenbao He [b,1], Chunlin Li [e,1], Shitong Zhao [b,1], Zhendong Li [b,1], Jing Wu [d], Junjun Li [f], Haichao Zhou [b,**], Yunfeng Yang [b,g,***], Yong Xu [a,*], Huitang Xia [c,d,****]

[a] Department of Thoracic Surgery, Shanghai Pulmonary Hospital, School of Medicine, Tongji University, Shanghai, China
[b] Department of Orthopedics, Shanghai Tongji Hospital, School of Medicine, Tongji University, Shanghai, China
[c] Department of Plastic Surgery, The First Affiliated Hospital of Shandong First Medical University & Shandong Provincial Qianfoshan Hospital, Jinan, Shandong, 250014, PR China
[d] Jinan Clinical Research Centre for Tissue Engineering Skin Regeneration and Wound Repair, The First Affiliated Hospital of Shandong First Medical University, Jinan, China
[e] Department of Orthopaedics, Qilu Hospital of Shandong University, Shandong University Centre for Orthopaedics, Advanced Medical Research Institute, Cheeloo College of Medicine, Shandong University, Jinan, China
[f] Department of Neurosurgery, Union Hospital, Tongji Medical College, Huazhong University of Science and Technology, Wuhan, China
[g] Department of Orthopaedics, Ruijin Hospital, Shanghai Jiao Tong University School of Medicine, Shanghai, China

ARTICLE INFO

*Keywords:*
Spatiotemporal control
Giant cell tumors of bone
Shell-core structure
Double-layered scaffold
Osteochondral regeneration

ABSTRACT

The osteochondral defects (OCDs) resulting from the treatment of giant cell tumors of bone (GCTB) often present two challenges for clinicians: tumor residue leading to local recurrence and non-healing of OCDs. Therefore, this study focuses on developing a double-layer PGPC-PGPH scaffold using shell-core structure nanofibers to achieve "spatiotemporal control" for treating OCDs caused by GCTB. It addresses two key challenges: eliminating tumor residue after local excision and stimulating osteochondral regeneration in non-healing OCD cases. With a shell layer of protoporphyrin IX (PpIX)/gelatin (GT) and inner cores containing chondroitin sulfate (CS)/poly(lactic-co-glycolic acid) (PLGA) or hydroxyapatite (HA)/PLGA, coaxial electrospinning technology was used to create shell-core structured PpIX/GT-CS/PLGA and PpIX/GT-HA/PLGA nanofibers. These nanofibers were shattered into nano-scaled short fibers, and then combined with polyethylene oxide and hyaluronan to formulate distinct 3D printing inks. The upper layer consists of PpIX/GT-CS/PLGA ink, and the lower layer is made from PpIX/GT-HA/PLGA ink, allowing for the creation of a double-layer PGPC-PGPH scaffold using 3D printing technique. After GCTB lesion removal, the PGPC-PGPH scaffold is surgically implanted into the OCDs. The sonosensitizer PpIX in the shell layer undergoes sonodynamic therapy to selectively damage GCTB tissue, effectively eradicating residual tumors. Subsequently, the thermal effect of sonodynamic therapy accelerates the shell degradation and release of CS and HA within the core layer, promoting stem cell differentiation into cartilage and bone tissues at the OCD site in the correct anatomical position. This innovative scaffold provides temporal control for anti-tumor treatment followed by tissue repair and spatial control for precise osteochondral regeneration.

Peer review under responsibility of KeAi Communications Co., Ltd.
* Corresponding author.
** Corresponding author.
*** Corresponding author. Department of Orthopedics, Shanghai Tongji Hospital, School of Medicine, Tongji University, Shanghai, China.
**** Corresponding author. Department of Plastic Surgery, The First Affiliated Hospital of Shandong First Medical University & Shandong Provincial Qianfoshan Hospital, Jinan, Shandong, 250014, PR China.
*E-mail addresses:* dr_zhouhaichao@163.com (H. Zhou), dr_yangyf123@163.com (Y. Yang), xuyong@tongji.edu.cn (Y. Xu), 3083@sdhospital.com.cn (H. Xia).
[1] These authors contributed equal to this work.

https://doi.org/10.1016/j.bioactmat.2023.12.020
Received 29 October 2023; Received in revised form 15 December 2023; Accepted 22 December 2023

## 1. Introduction

Giant cell tumor of bone (GCTB) is a borderline tumor known for its strong local aggressiveness [1]. Although its malignancy rate is low, at less than 1 %, its strong local invasiveness frequently results in severe bone and articular cartilage damage [2]. While local excision is generally recognized as the preferred treatment for GCTB, tumor recurrence often follows GCTB local curettage, with recurrence rates up to 40 % [3]. Postoperative radiotherapy and chemotherapy can reduce tumor recurrence to a certain extent but can also lead to complications such as normal tissue damage and adverse physiological reactions [4]. Another strategy to reduce tumor recurrence is extensive tumor resection, which can lead to massive osteochondral defects (OCDs) exceeding the body's self-healing capacity, including articular cartilage and subchondral bone tissues [5]. Therefore, effectively treating GCTB-induced OCDs is a significant clinical challenge that requires urgent solutions.

To address this challenge, two key conditions must be met: 1) The elimination of residual tumor after local excision to prevent recurrence before OCD reconstruction. 2) Inducing stem cells to differentiate into cartilage or bone at the OCD site in the correct anatomical position. In other words, the ideal treatment method should first achieve the complete elimination of the tumor, followed by precise osteochondral regeneration, to achieve anatomical and functional OCD reconstruction while minimizing the probability of tumor recurrence. Therefore, the development of a new therapeutic platform that combines GCTB ablation and integrated osteochondral reconstruction, allowing for the temporal and spatial regulation of anti-GCTB and osteochondral processes, is essential, known as "spatiotemporal regulation".

Recent advances in nanomaterials science, regenerative medicine, and oncology have led to the development of integrated therapies that are effective in combating tumors and promoting tissue reconstruction [6]. To achieve the spatiotemporal regulation of "first anti-tumor and then osteochondral regeneration", it is necessary to prepare a multifunctional and controllable biomaterial that releases anti-tumor factors first, and then releases growth-promoting factors for articular cartilage and subchondral bone regeneration. Coaxial electrostatic spinning with two or more polymers to form shell-core structured nanofibers provides an excellent structural and functional basis for the orderly release of bioactive factors [7]. Specifically, coaxial electrostatic spinning with shell-core structure can be prepared so that its shell layer material is loaded with antitumor drugs, and the core layer material is loaded with induced osteochondral regenerative factors. The antitumor drugs within shell material are exposed to the outermost layer to preferentially exert anti-tumor effects, and with the gradual degradation of the shell material, the core material is then gradually released osteochondral regenerative factors to promote osteochondral regeneration.

The primary challenge is selecting a reliable antitumor agent loaded into the shell of a shell-core structured nanofiber to eliminate residual tumors in the OCD region. Protoporphyrin IX (PpIX, and its structural formula is depicted in Fig. S1, Supplemental Information), an effective sonosensitizer, exerts a potent antitumor effect based on sonodynamic therapy (SDT), which has great potential in combating deep-seated tumors due to ultrasound's superior tissue penetration [8]. PpIX-based SDT can selectively target tumor cells with minimal invasion, making it a logical choice for loading into the shell of a shell-core structured nanofiber.

After the complete elimination of residual tumor, choosing suitable bioactive agents for osteochondral regeneration is another key scientific issue that needs to be addressed. Chondroitin sulfate (CS) [9] and hydroxyapatite (HA) [10] are representative potent bioactive factors that naturally promote chondrogenesis and osteogenesis of bone marrow stem cells (BMSCs), respectively. Considering the normal osteochondral tissue features upper articular cartilage and the underlying subchondral bone, the development of bioactive bilayer scaffolds that simultaneously regenerate both the cartilage and subchondral bone has been considered a desirable strategy. In recent years, advanced three-dimensional (3D) printing technology could develop an elaborate and finer bilayer scaffold with a tunable structural architecture to mimic native osteochondral tissue [11]. Most importantly, CS and HA can be correctly loaded into the 3D printed scaffolds to induce BMSCs differentiation to cartilage and bone respectively, thus accurately matching the anatomical structure of the osteochondral tissue, which is almost tailor-made for irregular GCTB-induced OCDs, achieving precise regeneration of cartilage and bone tissue with spatially regulated characteristics at the sites of OCDs.

In conclusion, to address the clinical challenges in treating GCTB-induced OCDs, this study proposes the use of coaxial electrostatic spinning technology based on commonly used gelatin (GT) and poly (lactic-co-glycolic acid) (PLGA) to prepare shell-core structured PpIX/GT-CS/PLGA and PpIX/GT-HA/PLGA nanofibers, with PpIX/GT as the outer shell and CS/PLGA and HA/PLGA as the inner cores, respectively. These nanofibers are sheared into short-staple nanofibers and dispersed into polyethylene oxide (PEO) and hyaluronan solutions to prepare printing "inks". PpIX/GT-CS/PLGA dispersed nanofibers serve as the ink of the upper layer, and PpIX/GT-HA/PLGA dispersed nanofibers serve as the ink of the lower layer. 3D printing is then employed to create a two-layer 3D porous scaffold, referred to as the PGPC-PGPH scaffold. After local resection of the GCTB lesion, the PGPC-PGPH scaffold is implanted into the OCDs. The acoustic sonosensitizers (PpIX) in the outer layer target and eliminate GCTB tissue under ultrasound, preventing tumor recurrence. As the outer shell degrades, the inducing factors (CS, HA) in the inner core promote the differentiation of stem cells into osteoblasts and chondroblasts, precisely repairing OCDs. The bilayer PGPC-PGPH scaffold provides temporal control for anti-tumor treatment followed by tissue repair and spatial control for precise osteochondral regeneration, laying the foundation for the clinical translation of "spatiotemporal regulation" in treating GCTB-induced OCDs (See Scheme 1 for an illustration of the concept).

## 2. Materials and methods

### 2.1. Preparation of shell-core structured PpIX/GT-CS/PLGA and PpIX/GT-HA/PLGA nanofibers

PpIX (Macklin, China) and GT (Sigma, USA) were dissolved in hexafluoroisopropanol (Macklin, China) at concentrations of 160 μM and 80 mg/mL, respectively. After magnetic stirring for 6 h, a homogeneous and transparent solution with the appropriate viscosity for the shell layer was obtained. Concurrently, CS (Macklin, China) and PLGA (Sigma, USA) were dissolved in hexafluoroisopropanol at concentrations of 10 mg/mL and 100 mg/mL, respectively. After another 6 h of magnetic stirring, a homogeneous and transparent solution with the suitable viscosity for the core layer was achieved.

The coaxial electrospinning process was performed under specific conditions, including a voltage range of 10.5–13.5 kV, a collector plate distance ranging from 8 to 14 cm, a core layer spinning solution flow rate of 0.5 mL/h, and a shell layer spinning solution flow rate of 0.1–0.9 mL/h. These conditions resulted in the production of PpIX/GT-CS/PLGA composite nanofibers. These membranes were initially cross-linked by exposure to a 25 % glutaraldehyde solution vapor for 3 h and then vacuum-dried at room temperature for 24 h. The same method was employed to prepare PpIX/GT-HA/PLGA nanofibers, with a concentration of 20 mg/mL for HA (Macklin, China). GT-PLGA nanofibers were identically prepared to serve as control. Specific components information involved in the fabrication of the PGPC-PGPH scaffolds were listed in Table. 1 (Supporting Information).

To examine the microstructure of GT-PLGA, PpIX/GT-CS/PLGA, and PpIX/GT-HA/PLGA nanofibers, scanning electron microscopy (SEM, FEI Inspect F50, USA) and transmission electron microscopy (TEM, JEOL JEM-F200, Japan) were utilized. ImageJ software was employed to calculate the average fiber diameter. Fourier-transform infrared spectroscopy (FTIR, Thermo Scientific, USA) was used to identify the

# Figure legends

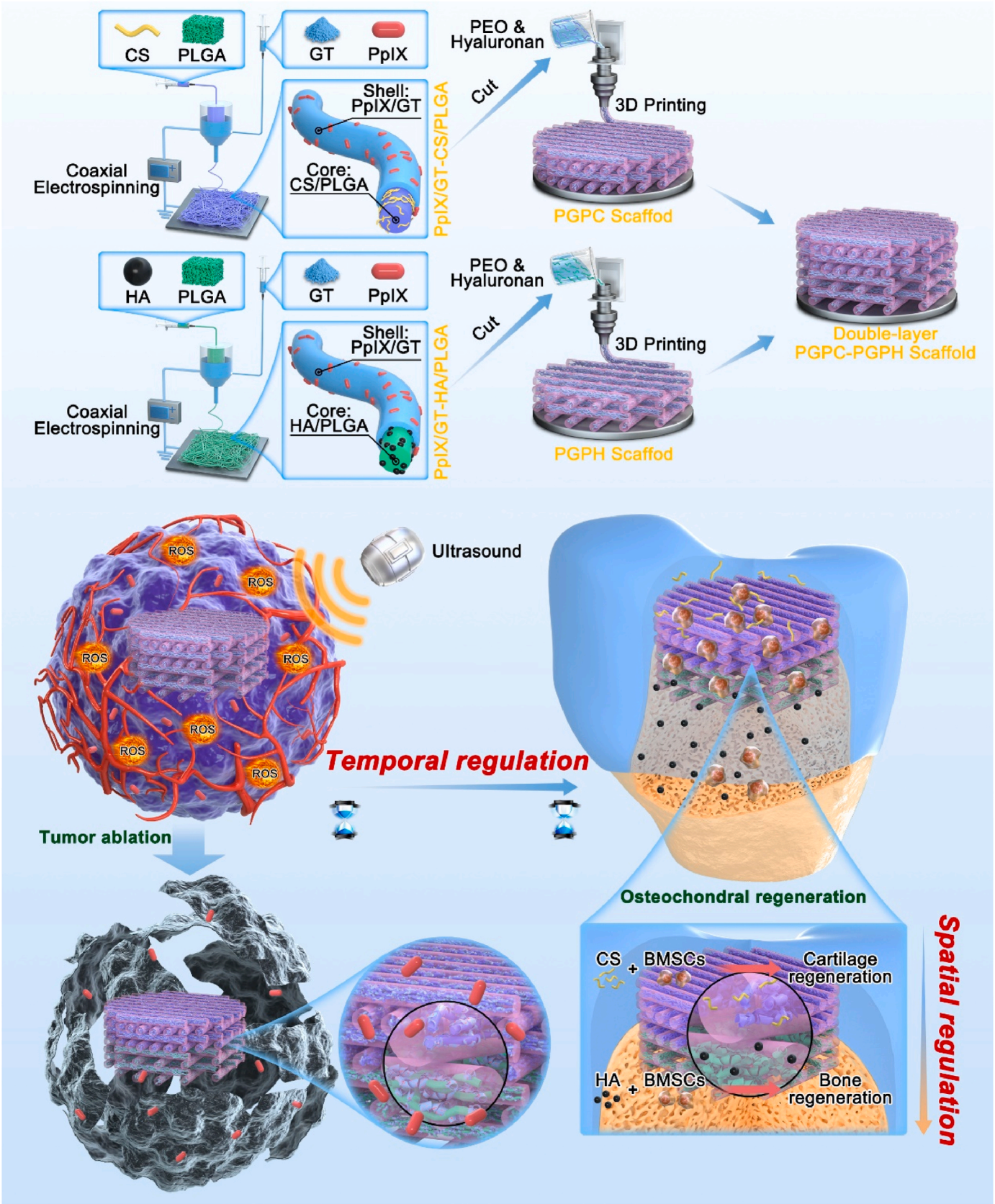


*(caption on next page)*

**Scheme 1. Outlines the experimental process.** In summary, we employed coaxial electrostatic spinning technology to fabricate nanofibers comprising PpIX/GT as the outer shell and CS/PLGA and HA/PLGA as the inner cores. Subsequently, we fragmented the PpIX/GT-CS/PLGA and PpIX/GT-HA/PLGA nanofibers into dispersed nanofibers and combined them with PEO and hyaluronan to produce 3D printable "inks". Using these inks, we conducted 3D printing to create a double-layer PGPC-PGPH porous scaffold, with the upper layer consisting of PpIX/GT-CS/PLGA ink and the lower layer comprising PpIX/GT-HA/PLGA ink. The sonosensitizer PpIX in the outer layer was employed to undergo SDT, selectively damaging GCTB tissue and effectively eliminating residual tumors. Subsequently, the thermal effect resulting from SDT expedited the release of CS and HA from the inner core layer, thereby promoting stem cell differentiation into cartilage and bone tissue, thus facilitating the repair of OCDs. This innovative scaffold not only allows for precise temporal control of anti-tumor treatment followed by tissue repair but also offers spatial control for accurate osteochondral regeneration.

components of PpIX, CS, and HA in the nanofibers. Mechanical tests were conducted to assess stress-strain curves, fracture strain, and Young's modulus for the three nanofibers.

### 2.2. Preparation of double-layered PGPC-PGPH porous scaffold

The prepared PpIX/GT-CS/PLGA and PpIX/GT-HA/PLGA nanofibers were cut into small 0.5 × 0.5 cm fragments. These fragments were immersed in deionized water and processed in a high-speed homogenizer (DR500 Std, USA) at 6000 rpm for 10 min to disperse the fragments into short fibers. SEM was used to observe the morphology of PpIX/GT-CS/PLGA and PpIX/GT-HA/PLGA short fibers, and ImageJ software was used to calculate the fibers' diameter.

Next, a 7 % solution of PEO (Sigma, USA) and a 5 % solution of hyaluronan (Sigma, USA) were prepared. 3 mL of the PEO solution and 2 mL of the hyaluronan solution were mixed with 5 g of the short fibers from PpIX/GT-CS/PLGA and PpIX/GT-HA/PLGA, respectively. Using a 3D printer (MAM-II FreeForm Fabrication System), PGPC-PGPH scaffolds were fabricated. The nozzle movement speed was set at 0.5 mm/s, and the extrusion speed was set at 0.0018 mm/s. The strand spacing (the distance between the middle lines of adjacent strands) was adjusted to 900 μm, while the layer slicing remained at 380 μm. The strand angle between subsequent layers was set at 90°. Subsequently, using PpIX/GT-CS/PLGA solution as the upper layer printing "ink" and PpIX/GT-HA/PLGA solution as the lower layer printing "ink", a double-layer porous PGPC-PGPH scaffold (with a diameter of 4 mm and height of 4 mm) was printed. In addition, single-layer porous GP, PGPC, and PGPH scaffolds were similarly printed using separate GT-PLGA, PpIX/GT-CS/PLGA, and PpIX/GT-HA/PLGA nanofibers.

The printed porous scaffolds underwent thorough cross-linking by immersing them in a solution containing 1-Ethyl-3-(3′-dimethylaminopropyl) carbodiimide (EDC) and N-Hydroxysuccinimide (NHS) (5 % EDC, 3 % NHS, 95 % ethanol, Macklin, China) for 24 h. The final printed scaffolds were obtained through freeze-drying.

The macroscopic appearance and microscopic structure of the PGPC, PGPH, and PGPC-PGPH scaffolds were observed. Mechanical tests were conducted using an E42 universal testing machine (MTS, USA) to evaluate stress-strain curves and Young's modulus for GP, PGPC, PGPH, and PGPC-PGPH scaffolds [12]. The scaffolds were compressed at a rate of 2.00 mm/min to reach a strain of 95 %, and stress-strain curves were obtained. Young's modulus was calculated based on these curves. For cyclic compression tests, the scaffolds were fully wetted in phosphate-buffered saline (PBS, Macklin, China) and compressed to a strain of 60 % at a rate of 2.00 mm/min, then returned to 0 %, with each sample undergoing 100 repetitions to observe changes in stress-strain curves during repeated compression for PGPC, PGPH, and PGPC-PGPH scaffolds.

Ultrasound at a frequency of 2.5 MHz was applied to GP, PGPC, PGPH, and PGPC-PGPH printed scaffolds soaked in 8 mL of PBS with ultrasound treatment for 60 s. Temperature changes were observed in each group of scaffolds, and the content of PpIX in PBS of PGPC, PGPH, and PGPC-PGPH groups was measured at different time points (0, 10, 20, 30, 40, 50, 60 s). Subsequently, the temperature of nanofibers in control, GT-PLGA, PpIX/GT-PLGA, PpIX/GT-CS/PLGA, and PpIX/GT-HA/PLGA groups was also subjected to ultrasound at a frequency of 2.5 MHz was applied to them for 60 s. Then, the printed PGPC, PGPH, and PGPC-PGPH scaffolds soaked in PBS were subjected to ultrasound treatment at different intensities (0, 0.5, 1, 1.5, 2, 2.5 MHz) for 60 s, and changes in the PpIX content in PBS for each group were measured. Finally, ultrasound at a frequency of 2.5 MHz was applied to PGPC-PGPH scaffolds soaked in PBS for 60 s, and then maintain the same operation another 15 days to measure the changes in the content of PpIX, CS, and HA every two days. The PGPC-PGPH scaffolds soaked in PBS without ultrasonic irradiation was served as a control group.

### 2.3. Evaluation of cytocompatibility for double-layered PGPC-PGPH scaffold

The primary BMSCs (purchased from Shanghai Cell Storage Center, China) with a concentration of $10^6$ cells/mL were co-cultured for 4 days with the following substrates: an empty culture dish (serving as the control group) or with printed GP-GP, PGPC-PGP, PGP-PGPH, and PGPC-PGPH scaffolds. On the 1st and 4th days following cell seeding, several assessments were performed to evaluate the cytocompatibility of the printed scaffolds with BMSCs. These assessments included live-dead cell staining (Invitrogen, USA), phalloidin staining, and cell viability measurements using a Cell Counting Kit-8 cell viability assay kit (CCK-8, Dojindo, Japan).

### 2.4. Ex vivo evaluation of the cytotoxic effect of PpIX-Loaded nanofibers and printed scaffolds on GCTB cells upon ultrasound irradiation

The primary GCT0404 human GCTB cell line, obtained from the Shanghai Cell Storage Center in China and with a concentration of $10^6$ cells/mL, was co-cultured under various conditions. These conditions included an empty culture dish (serving as the control group), GT-PLGA, GT-CS/PLGA, GT-HA/PLGA, PpIX/GT-PLGA, PpIX/GT-CS/PLGA, and PpIX/GT-HA/PLGA nanofibers, as well as printed GP-GP, GPC-GP, GP-GPH, PGP-PGP, PGPC-PGP, PGP-PGPH scaffolds. Each of these co-cultures was subjected to ultrasound irradiation with an intensity of 2.5 MHz and a duration of 60 s. Cell damage in each group was assessed through live-dead cell staining and cell viability assays.

Furthermore, in order to explore the optimal protocols for killing GCTB cells based on the PGPC-PGPH scaffold under ultrasound irradiation, GCTB-loaded nanofibers in PpIX/GT-PLGA, PpIX/GT-CS/PLGA, and PpIX/GT-HA/PLGA groups, as well as printed scaffolds in PGP-PGP, PGPC-PGP, PGP-PGPH, and PGPC-PGPH groups, were subjected to ultrasound with different treatment times (10, 20, 30, 40, 50, 60 s) and ultrasound intensity (0.5, 1.0, 1.5, 2.0, 2.5, 3.0 MHz). Cell viability was assessed using the CCK-8 kit in these conditions.

### 2.5. Cytotoxicity mechanism of PpIX-Loaded nanofibers and printed scaffolds to GCTB cells upon ultrasound

GCTB cells with a density of $10^6$ cells/mL were seeded onto various nanofibers (including control, GT-PLGA, PpIX/GT-PLGA, PpIX/GT-CS/PLGA, and PpIX/GT-HA/PLGA) and various printed double-layered scaffolds (GP-GP, PGP-PGP, PGPC-PGP, PGP-PGPH, and PGPC-PGPH), and were then subjected to 2.5 MHz ultrasound for 50 s. Thereafter, these treated samples were subjected to immunofluorescence reactive oxygen species staining (ROS) [13], and the ROS intensity was calculated from the obtained image. To further detect apoptotic cells, a flow cytometry examination was conducted using the previously established methods [14].

In addition, the mitochondrion of the above-treated GCTB cells were labeled with Rhodamine 123 (Sigma, USA), and then subjected to an inverted confocal laser scanning microscopy (CLSM, Keyence, Japan) to observe the dual-channel fluorescence imaging positions of Rhodamine 123 at 507 nm and PpIX at 405 nm.

Furthermore, the expression of apoptosis-related proteins (cytochrome *c*, Bax, and caspase-3) in the above treated GCTB cells were observed using immunofluorescence staining and Western blot (WB) examination [15]. The corresponding cytochrome *c*, Bax, and caspase-3 intensity were calculated based on the obtained images using immunofluorescence staining via an ImageJ software.

### 2.6. In vitro osteogenic and chondrogenic differentiation capacity of nanofibers and printed scaffolds to BMSCs

BMSCs, at a density of $10^6$ cells/mL, were seeded on various nanofibers (control, GT-PLGA, PpIX/GT-PLGA, PpIX/GT-CS/PLGA, and PpIX/GT-HA/PLGA) and printed double-layered scaffolds (GP-GP, PGP-PGP, PGPC-PGP, PGP-PGPH, and PGPC-PGPH). They were cultured in standard medium for 14 days. Subsequently, the expression of osteogenic-related genes (*Collagen I* (*Col1a1*), *osteocalcin* (*OCN*), and *Runt-related transcription factor 2* (*RUNX2*)) and chondrogenic-related genes (*Collagen II* (*Col2a1*), *SOX9*, and *aggrecan*) was analyzed using quantitative Polymerase Chain Reaction (qPCR) as previous established method [16], the detail primer sequences refer to Table 2 (Supplemental Information).

In addition, alkaline phosphatase staining (ALP, Sigma, USA) and Alizarin Red staining (Sigma, USA) were used to assess the enzymatic activity of mature osteoblast markers and visualize calcium salt deposition on cell surfaces. ALP activity was quantified using an AKP/ALP kit (Cyagen, Guangzhou, China), and Alizarin Red intensity was determined through ImageJ software analysis.

Furthermore, immunofluorescence staining was used to examine the expression of aggrecan and glycosaminoglycan (GAG). Aggrecan/DNA and GAG/DNA were quantified based on images obtained from immunofluorescence staining using ImageJ software.

Additionally, BMSCs, at a density of $10^6$ cells/mL, were similarly seeded on various printed single-layered scaffolds, including the control, PGP, PGPC, and PGPH. They were cultured for 21 days, and the retrieved samples were subjected to immunofluorescence COL I and OCN staining for osteogenic evaluation, as well as Safranin-O and immunohistochemical type II collagen (COL II) staining for chondrogenic evaluation.

### 2.7. Antitumor effect of printed scaffolds in GCTB-derived tumor-bearing nude mice

All animal experiments were approved by the Ethics Committee of Shanghai Pulmonary Hospital. A total of 25 nude mice (aged 4 weeks, weighing approximately 25 g) were obtained from Slaccas Experimental Animal Co., Ltd (Shanghai, China). They were randomly divided into five groups (control, GP-GP, PGPC-PGP, PGP-PGPH, and PGPC-PGPH) with 5 mice in each group.

GCTB cells, at a density of $5 \times 10^4$ cells/μL, were subcutaneously injected into the mice, and cultured for 7 days to establish a tumor-bearing nude mice model. Ultrasound irradiation at a 2.5 MHz intensity for 50 s was used for tumor ablation every day. The mice were monitored for body weight and tumor volume every two days for 14 days. At the end of the 14th day, the mice were sacrificed, and tumor samples were collected. Tumor weight was measured, and the samples were subjected to immunofluorescence ROS staining, hematoxylin and eosin (H&E) staining, immunohistochemical Ki-67, and TUNEL staining. TUNEL and Ki-67 intensities were calculated based on images obtained from immunohistochemical Ki-67 and TUNEL staining using ImageJ software.

### 2.8. Therapeutic effect of PGPC-PGPH scaffolds for spatially controlled osteochondral restoration in a rabbit OCD model

A total of 25 female New Zealand white rabbits, aged 3 months, weighing 2.5 kg, were randomly divided into five groups (blank, GP-GP, PGPC-PGP, PGP-PGPH, and PGPC-PGPH) with 5 rabbits in each group. An OCD model was established by drilling a 4 mm diameter hole at the center of the distal femoral articular surface in the left knee joint of each rabbit, with a depth of approximately 4 mm. The printed double-layered scaffolds were individually implanted into the OCDs of the rabbits, while the blank group received no scaffold implantation.

After 8 weeks, rabbit knee OCD samples were collected and examined macroscopically to determine the International Cartilage Repair Society (ICRS) score (The detail refer to Table 3, Supplemental Information). Micro-computed tomography (Micro-CT) was used to obtain 2D and 3D reconstruction images, as well as to quantify bone volume fraction (BV/TV) and trabecular thickness (Tb.Th). The immunofluorescence staining of COL I and OCN expression to characterize the osteochondral repair.

The samples were then sectioned, and regeneration of bone and cartilage tissue characteristics was observed through H&E staining, Safranin-O/Fast Green (SO/FG) staining, toluidine blue staining, and immunohistochemical COL II staining. The O'Driscoll histological score was determined based on the histological images (The detail refer to Table 4, Supplemental Information).

### 2.9. Statistical analysis

Statistical analysis was performed using GraphPad Prism 8.0. The results are presented as mean ± standard deviation, and data were analyzed using one-way analysis of variance. The level of statistical significance was set at $^*P < 0.05$.

## 3. Results and discussion

### 3.1. Preparation and characterization of shell-core structured PpIX/GT-CS/PLGA and PpIX/GT-HA/PLGA nanofibers

Coaxial electrospinning is widely used for creating shell-core structured biomaterials. It involves injecting shell and core layer solutions into coaxial capillary tubes with different inner diameters. At the nozzle's end, these solutions solidify into composite nanofibers under the influence of an electric field [17]. In this study, we employed coaxial electrospinning to produce shell-core structured PpIX/GT-CS/PLGA and PpIX/GT-HA/PLGA nanofibers. SEM images revealed that GT-PLGA, PpIX/GT-CS/PLGA, and PpIX/GT-HA/PLGA nanofibers all exhibited similar fibrous structures (Fig. 1A), indicating that the introduction of PpIX, CS, and HA did not affect the electrospinning process of GT-PLGA. TEM imaging further confirmed the presence of a clear shell-core structure in all three types of nanofibers. PpIX was dispersed in the lighter-colored GT "shell" while CS and HA mixed with PLGA in the darker-colored "core" (Fig. 1B).

The FTIR spectrum demonstrated the coexistence of GT and PLGA in the GT-PLGA samples, PpIX and CS in the PpIX/GT-CS/PLGA samples, and PpIX and HA in the PpIX/GT-HA/PLGA samples, verifying the successful loading of PpIX, CS, and HA into the GT-PLGA nanofibers (Fig. 1C). Diameter measurements indicated that GT-PLGA, PpIX/GT-CS/PLGA, and PpIX/GT-HA/PLGA nanofibers had similar diameters, approximately 0.4 μm (ranging from 0.1 to 1.0 μm) (Fig. 1D). Data from mechanical testing revealed that PpIX/GT-CS/PLGA and PpIX/GT-HA/PLGA nanofibers exhibited similar stress-strain curves, fracture characteristics, and Young's modulus (Fig. 1E–G). This suggests that PpIX/GT-CS/PLGA and PpIX/GT-HA/PLGA nanofibers are suitable for tissue engineering applications.

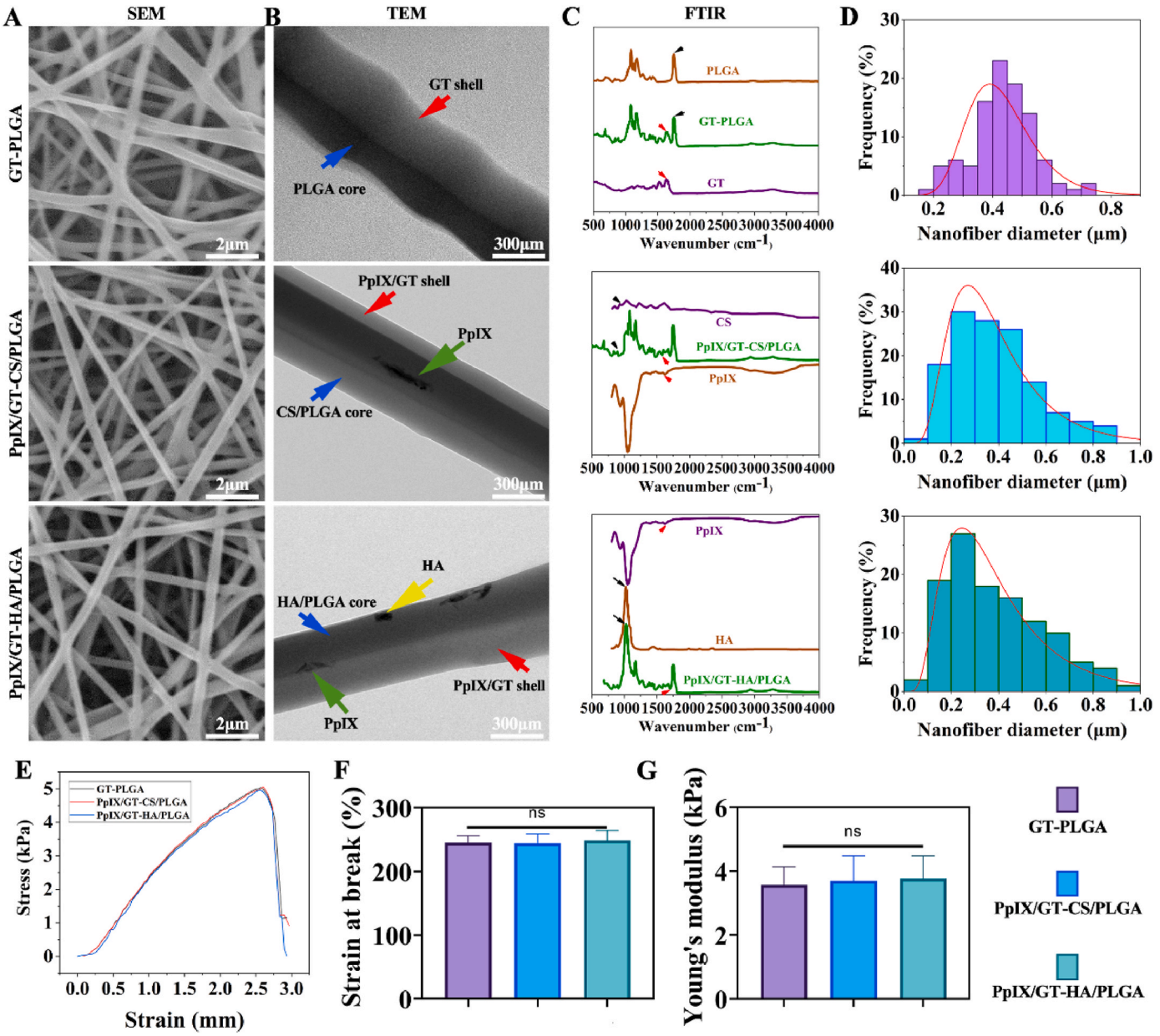


**Fig. 1.** Illustrates the preparation of GT-PLGA, PpIX/GT-CS/PLGA, and PpIX/GT-HA/PLGA nanofibers. A) SEM and B) TEM images reveal GT-PLGA, PpIX/GT-CS/PLGA, and PpIX/GT-HA/PLGA nanofibers. In these images, red arrows indicate the presence of GT or PpIX/GT shells, green arrows represent PpIX within PpIX/GT shells, blue arrows denote PLGA, CS/PLGA, or HA/PLGA cores, and yellow arrows highlight HA within the HA/PLGA core. C) The FTIR spectrum for GT-PLGA, PpIX/GT-CS/PLGA, and PpIX/GT-HA/PLGA samples is provided. D) Diameter analysis of GT-PLGA, PpIX/GT-CS/PLGA, and PpIX/GT-HA/PLGA nanofibers is displayed. E) The stress curve, F) strain at break, and G) Young's modulus for GT-PLGA, PpIX/GT-CS/PLGA, and PpIX/GT-HA/PLGA samples are presented. "ns" indicates no statistical significance.

### *3.2. 3D printing of bilayer PGPC-PGPH porous scaffold*

To create the "ink" for 3D printing, we initially processed the prepared PpIX/GT-CS/PLGA and PpIX/GT-HA/PLGA nanofibers into finely shredded nanofibers using a high-speed homogenizer. This step aimed to produce nanofibers with a uniform morphology and small enough to facilitate 3D printing. SEM images showed that the composite nanofiber membranes were dispersed into numerous similarly sized short nanofibers with diameters ranging between 110 and 150 μm and an average of approximately 130 μm (Fig. 2A).

Subsequently, we soaked these short nanofibers in PEO and hyaluronan solutions to achieve a suitable viscosity for 3D printing. It was crucial to achieve high viscosity in the dispersion fluid by maximizing the content of nanofibers while maintaining appropriate quantities of PEO and hyaluronan solutions to avoid affecting the nanofiber morphology of the 3D scaffold [18,19]. After parameter exploration, we found that a mixture of 3 ml PEO solution, 2 ml hyaluronan solution, and 5 g of nanofibers formed stable, uniform "ink" that could be consistently extruded using a syringe (Fig. 2B).

Using 3D printing technology, we successfully created the double-layered PGPC-PGPH porous scaffold, with PGPC as the upper layer and PGPH as the lower layer. The scaffold had a cylindrical structure with a diameter of 4 mm and a height of 4 mm (Fig. 2C). Under SEM, the PGPC-PGPH scaffold exhibited a 3D porous structure with a nanofiber diameter of approximately 500 μm, and the two layers (upper and lower) were closely connected (Fig. 2D).

To enhance the mechanical properties and ensure better binding of the nano-scaled fibers in the PGPC-PGPH scaffold, we used EDC for

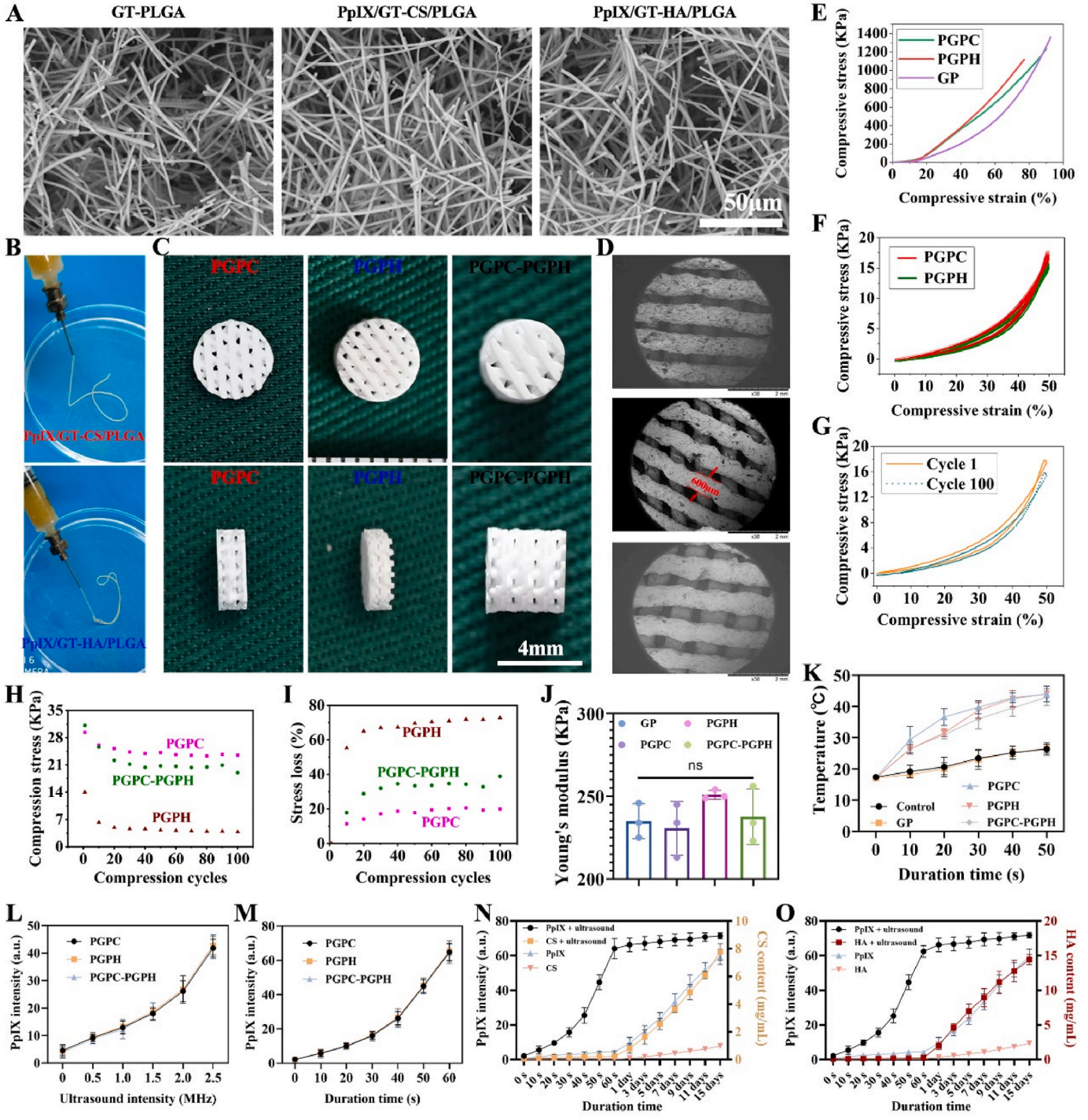


**Fig. 2.** Depicts the process of creating the 3D printed double-layer PGHC-PGPH scaffold. A) SEM images of cut GT-PLGA, PpIX/GT-CS/PLGA, and PpIX/GT-HA/PLGA fibers are presented. B) A photograph showcases PpIX/GT-CS/PLGA and PpIX/GT-HA/PLGA inks, dissolved in a solution of PEO and hyaluronan, extruded from needles. C) A photograph exhibits the PGPC, PGPH, and double-layered PGHC-PGPH scaffolds. D) SEM images illustrate the structures of PGPC, PGPH, and the double-layered PGHC-PGPH scaffolds. E) Compressive stress-strain curves of GP, PGPC, and PGPH scaffolds are displayed. F) Compressive stress-strain curves for PGPC and PGPH scaffolds subjected to 100 cycles of compressive testing at 50 % strain are shown. G) Compressive stress-strain curves are presented for the double-layered PGHC-PGPH scaffold at 1 and 100 cycles of compressive testing at 60 % strain. H–I) The historical data of maximum stress and stress loss in relation to multiple compressive cycles is provided. J) Young's modulus values are presented for GP, PGPC, PGPH, and the double-layered PGHC-PGPH scaffolds. K) The temperature of samples in Control, GP, PGPC, PGPH, and PGPC-PGPH groups during ultrasonic irradiation with varying durations is illustrated. L-M) PpIX intensity in PGPC, PGPH, and the double-layered PGHC-PGPH scaffolds upon ultrasonic irradiation with varying ultrasonic intensity and duration is shown. N–O) The release of CS and HA from double-layered PGHC-PGPH scaffolds upon immersion in PBS with and without ultrasonic irradiation with varying time durations is demonstrated.

cross-linking intentionally. The concentration of EDC used was 5 g/L, and the free amino acid number was reduced from about 32.5 % initially to about 15 % at the completion of cross-linking. EDC cross-linked both hyaluronan and GT in the scaffold and formed cross-links between the carboxyl groups of hyaluronan and the residual amino groups in GT, ensuring strong adhesion between the fibers and the formation of an integrated scaffold with specific mechanical strength [20]. Compressive stress-strain curves for the single-layered GP, PGPC, and PGPH scaffolds exhibited similar compressive mechanical properties (Fig. 2E) and remained stable after 100 repeated compression cycles (Fig. 2F). The double-layered PGPC-PGPH scaffold also maintained consistent mechanical properties during 100 compression cycles (Fig. 2G). The cyclic

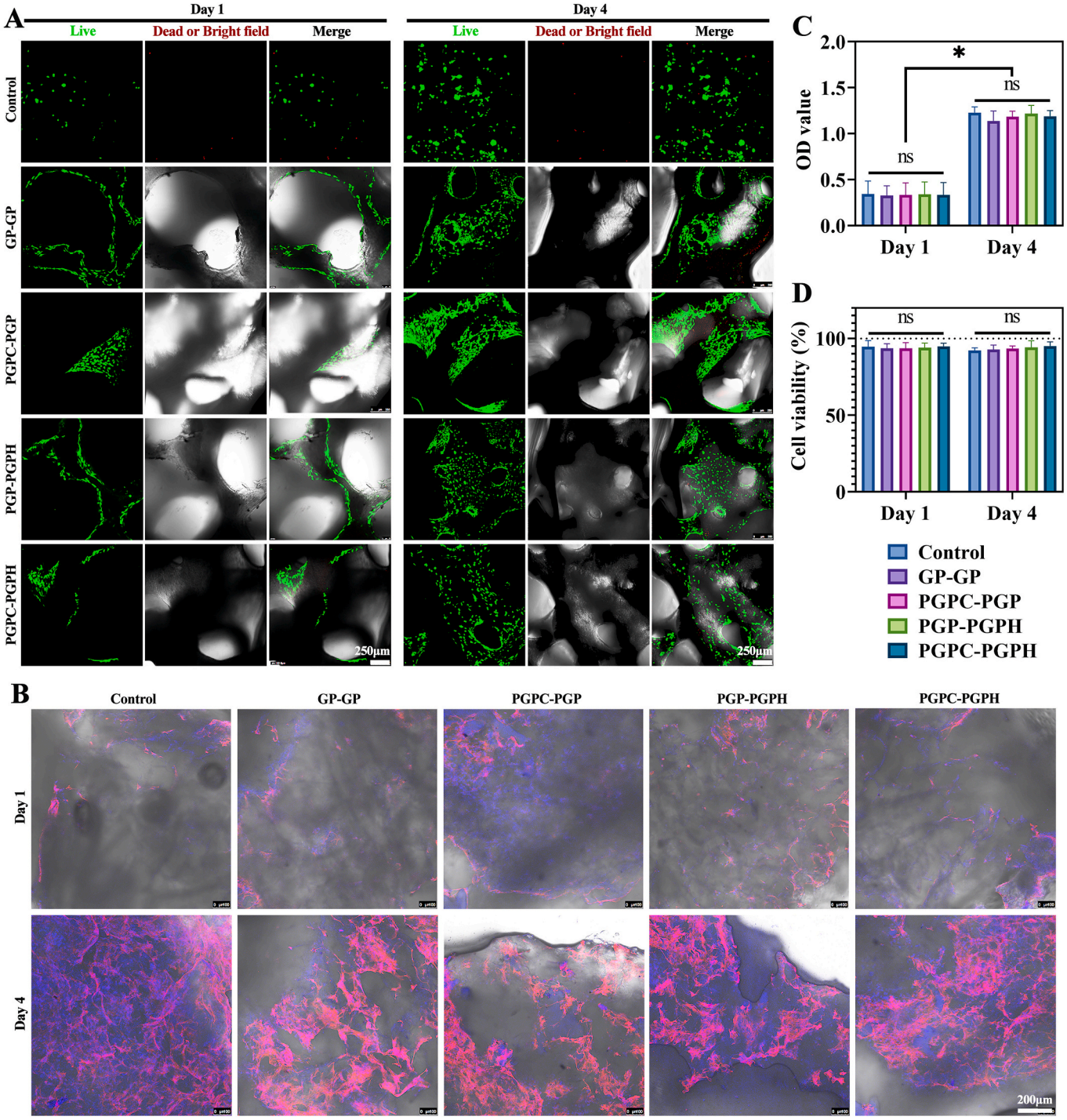


**Fig. 3.** Displays the results of in vitro cytocompatibility assessments of 3D printed scaffolds co-cultured with BMSCs for 1–4 days. A) Live/dead staining of BMSCs on 3D printed Control, PGP-PGP, PGPC-PGP, PGP-PGPH, and PGPC-PGPH scaffolds at day 1 and 4. In these images, the left panels depict live cells stained in green, the middle panels show dead cells stained in red (for the control group) or are represented in bright field (for PGP-PGP, PGPC-PGP, PGP-PGPH, and PGPC-PGPH groups), and the right panels display merged images of the left and middle images. B) Nuclei and cytoskeleton staining of BMSCs cultured on different groups at day 1 and 4 are provided. In these images, nuclei are stained in blue, and the cytoskeleton is stained in red. C) OD values obtained via a CCK-8 assay for BMSCs cultured on each group at day 1 and 4 are presented. D) Cell viability of BMSCs cultured on each group at day 1 and 4 is shown. Significance denoted by * indicates $p < 0.05$, while "ns" represents no statistical significance.

compression test showed a loss of stress, resulting in a significant decrease in the maximum stress for the PGPC, PGPH, and PGPC-PGPH scaffolds (Fig. 2H and I), indicating the elasticity of the printed PGPC-PGPH scaffold, making it suitable for use as a biological scaffold for OCDs regeneration [21]. The Young's modulus of all the printed scaffolds exceeded 200 KPa (Fig. 2J), meeting the mechanical strength requirements for OCDs regeneration [22].

The PGPC-PGPH scaffold should effectively release PpIX, CS, and HA to achieve the desired anti-tumor and OCDs regeneration abilities. Therefore, we investigated the impact of ultrasound on the release of various bioactive factors within the printed scaffold. Our results showed that: 1) With increasing ultrasound exposure time, the nanofiber groups containing PpIX exhibited a faster temperature increase compared to the groups without PpIX, indicating a thermal effect of PpIX upon ultrasound (Figs. S3A–B, Supporting Information). The printed scaffolds containing PpIX exhibited an enhanced heating effect compared to the groups without PpIX when excited by ultrasound (Fig. 2K). 2) Both the intensity of ultrasound and the exposure time accelerated the release of PpIX within the printed scaffold (Fig. 2L-M). 3) Extended ultrasound exposure allowed for the prior gradual release of PpIX located in the "shell layer" during the initial 60 s, followed by the released of CS and HA within the "core layer" from 1 to 15 days (Fig. 2N-O). Notably, obviously accelerated releases of CS and HA were observed in the ultrasound-treated group compared to the control group, indicating the heat generated by PpIX during cavitation under low-frequency ultrasound promoted the disintegration of the shell layer of the nanofibers [23]. As a consequence, the sustained controlled release behavior of the 3D scaffolds suggests the potential to maintain the efficacy of sonodynamic therapy against GCTB for a minimum of 15 days.

### 3.3. Cytocompatibility of the printed double-layered PGPC-PGPH scaffold

A regenerative scaffold must demonstrate excellent biocompatibility for its successful use in tissue engineering. Both GT and PLGA [24], as scaffold materials, and HA [25] and CS [26], as bioactive factors for osteochondral induction, have been extensively studied and are known to possess excellent cytocompatibility. Furthermore, PpIX, chosen as an ideal sonosensitizer, offers various advantages, including chemical purity, low toxicity, rapid clearance from the body, and importantly, it is non-cytotoxic in the absence of ultrasound [27]. Thus, we intentionally selected these materials for the treatment of GCTB-derived OCDs.

In this study, we co-cultured BMSCs with the printed scaffolds to evaluate their cytocompatibility. Live/dead cell and phalloidin staining revealed that BMSCs in all groups (including the control, as well as printed GP-GP, PGPC-PGP, PGP-PGPH, and PGPC-PGPH scaffolds) were successfully seeded within the scaffold, continued to proliferate over 1–4 days, and exhibited high cell viability with negligible dead cells (Fig. 3A and B). Quantitative data from the CCK-8 assay (Fig. 3C) further confirmed an increasing trend in optical density (OD) values from 1 to 4 days, and cell viability (Fig. 3D) remained high (approximately 100 %) in all five groups. Overall, the printed double-layered PGPC-PGPH scaffold demonstrated excellent biocompatibility, laying a solid foundation for subsequent therapeutic applications.

### 3.4. Ex vivo antitumor effects of PGPC-PGPH scaffold upon ultrasound irradiation

Considering that the printed PGPC-PGPH scaffold is intended to eliminate GCTB cells, we investigated the ex vivo antitumor effect of the printed PGPC-PGPH scaffold when co-cultured with GCTB cells under ultrasound irradiation. Live/dead cell staining indicated that non-PpIX-containing groups, including nanofibers (control, GT-PLGA, GT-CS/PLGA, and GT-HA/PLGA) and printed scaffolds (GP-GP, GPC-GP, GP-GPH), exhibited no cytotoxicity to GCTB cells under ultrasound, with negligible dead cells. In contrast, PpIX-containing groups, including nanofibers (PpIX/GT-PLGA, PpIX/GT-CS/PLGA, and PpIX/GT-HA/PLGA) and printed scaffolds (PGP-PGP, PGPC-PGP, PGP-PGPH, and PGPC-PGPH), showed significant cytotoxic effects on GCTB cells following ultrasound treatment (Fig. 4A and B). Cell viability assay results further confirmed these observations (Fig. 4C and D).

Subsequently, we explored the optimal protocols for killing GCTB cells based on the PGPC-PGPH scaffold under ultrasound irradiation. The results showed that cell viability decreased as the duration of ultrasound exposure increased from 0 to 50 s and ultrasound intensity increased from 0 to 2.5 MHz, both in different nanofibers (PpIX/GT-PLGA, PpIX/GT-CS/PLGA, PpIX/GT-HA/PLGA) and printed scaffolds (PGP-PGP, PGPC-PGP, PGP-PGPH, and PGPC-PGPH). However, no further changes were observed beyond 50 s duration and 2.5 MHz intensity (Figure S4A-B and S5A-B, Supporting Information). In summary, SDT combined with PpIX-loaded printed scaffolds had a significant killing effect on ex vivo GCTB cells.

It's worth noting that while ultrasound can continuously deliver energy to cells in the irradiation area, excessive energy absorption due to prolonged ultrasound exposure can lead to mechanical damage or cell death in healthy cells. On the other hand, insufficient ultrasound intensity and time may not achieve the desired therapeutic effect. Therefore, personalized optimization of ultrasound intensity and exposure time is crucial before using sonodynamic therapy to treat various tumor cells. The study identified an optimal ultrasound intensity of 2.5 MHz and an exposure time of 50 s as the conditions for achieving the best results.

### 3.5. Mechanisms of PGPC-PGPH scaffold induced GCTB cell death upon ultrasound irradiation

Previous studies have established that SDT primarily employs low-intensity ultrasound to stimulate a diseased area, activating photosensitizers that accumulate there. This activation leads to the generation of reactive oxygen species (ROS). The buildup of intracellular ROS triggers a series of cellular events, including a reduction in mitochondrial membrane potential, cytoskeletal contraction, chromatin condensation, membrane rupture, and DNA fragmentation. These events ultimately lead to the apoptosis of diseased cells [28].

In our study, immunofluorescence ROS staining of treated GCTB cells under ultrasound irradiation indicated that groups without PpIX (Control and GT-PLGA nanofibers and GP-GP printed scaffold) exhibited minimal ROS green fluorescence, while PpIX-loaded groups (PpIX/GT-PLGA, PpIX/GT-CS/PLGA, and PpIX/GT-HA/PLGA nanofibers, as well as PGP-PGP, PGPC-PGP, PGP-PGPH, and PGPC-PGPH printed scaffolds) showed a significant increase in ROS production (Fig. 5A–B and E-F). Flow cytometry analysis of treated GCTB cells in groups without PpIX showed very few dead cells and almost no apoptotic cells, whereas PpIX-loaded groups displayed varying levels of apoptosis and a small number of dead cells (Fig. 5C–D and G-H).

Furthermore, dual-channel fluorescence images through confocal laser scanning microscopy (CLSM) were used to observe the localization of PpIX and GCTB cell mitochondria. The released PpIX (stained in red) from PpIX-loaded groups was found to overlap with the Rhodamine 123 labeled mitochondria (stained in green), indicating that PpIX was primarily localized in the mitochondria of GCTB cells (Fig. 5I and Figs. S6–7, Supporting Information).

Immunofluorescence staining and quantified data for cell apoptosis-related proteins in each group also supported these findings. The groups without PpIX exhibited minimal fluorescence for cytochrome *c*, Bax, and caspase-3, while the PpIX-loaded groups showed significantly higher fluorescence (Fig. 5J and Figure S8 and S9A-F, Supporting Information). WB results for apoptosis-related proteins in each group were consistent with the above experiments (Figs. S10A–B, Supporting Information).

In summary, PpIX, in combination with ultrasound, significantly increased ROS production in GCTB cells, leading to cell apoptosis. The mechanism involves PpIX entering the mitochondria of GCTB cells, being activated under ultrasound influence, and generating cavitation

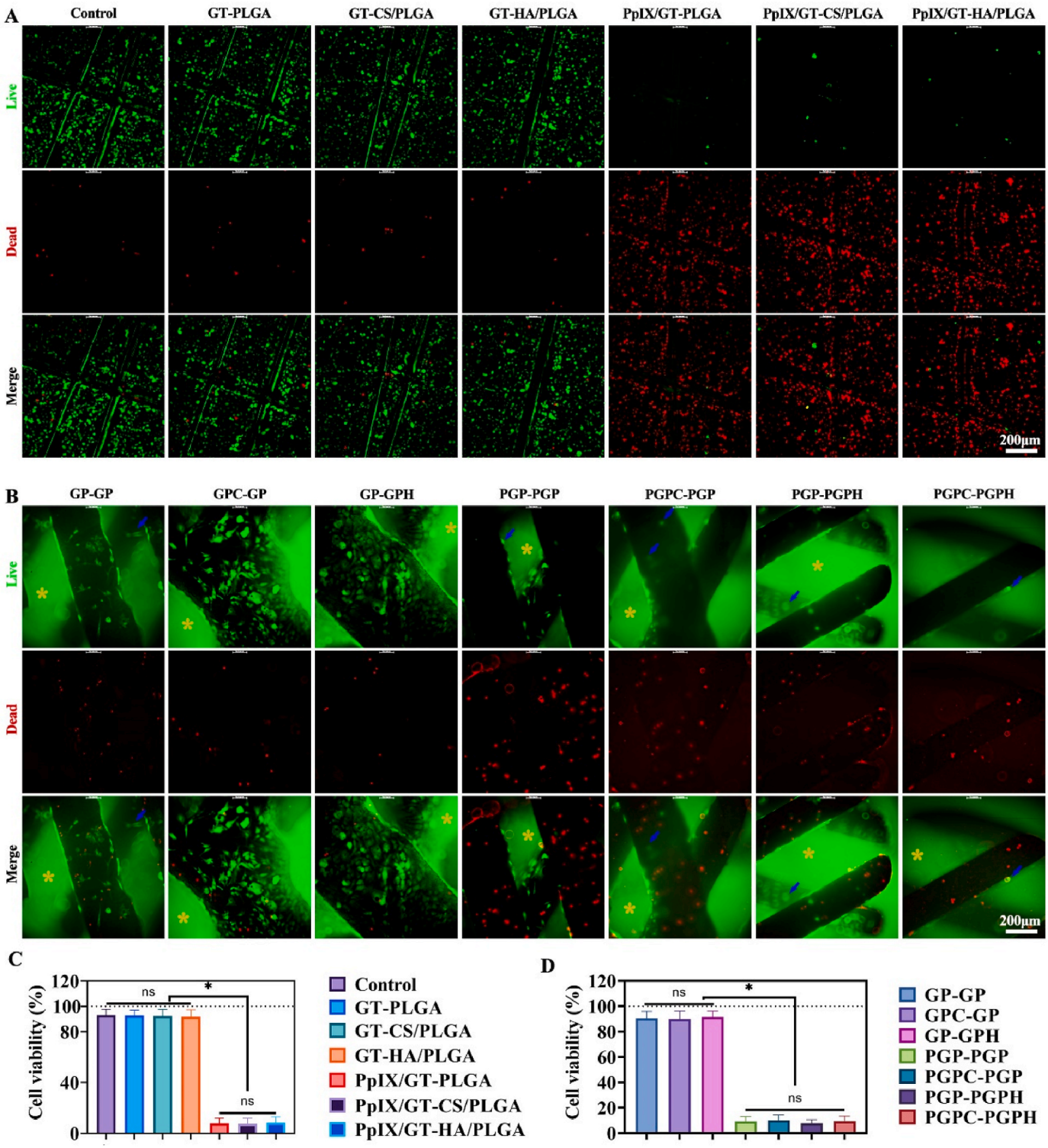


**Fig. 4.** Illustrates the results of in vitro cytotoxicity assessments for nanofibers and 3D printed scaffolds under ultrasound irradiation. A) Live/dead staining images and C) cell viability data are presented for Control, GT-PLGA, GT-CS/PLGA, GT-HA/PLGA, PpIX/GT-PLGA, PpIX/GT-CS/PLGA, and PpIX/GT-HA/PLGA nanofibers. B) Live/dead staining images and D) cell viability data are provided for printed GP-GP, GPC-GP, GP-GPH, PGP-PGP, PGPC-PGP, PGP-PGPH, and PGPC-PGPH scaffolds. Blue arrows indicate GCTB cells. Yellow marked "*" indicate non-specific staining of the scaffolds. Significance is denoted by *, indicating $p < 0.05$, while "ns" represents no statistical significance.

effects. This activation also transfers its excitation energy to surrounding ground-state oxygen molecules, resulting in a significant ROS increase [29]. ROS accumulation triggers several events: 1) Oxidation of adjacent residues in the adenine nucleotide translocase of the mitochondrial inner membrane, leading to mitochondrial permeability transition pore opening, disrupting mitochondrial transmembrane potential, and releasing cytochrome *c* from the mitochondria [30]. 2) Promotion of lysosomal release of hydrolytic enzymes, subsequently activating the cytosolic Bax complex, which forms a calcium channel between the endoplasmic reticulum and the mitochondrial outer membrane, leading

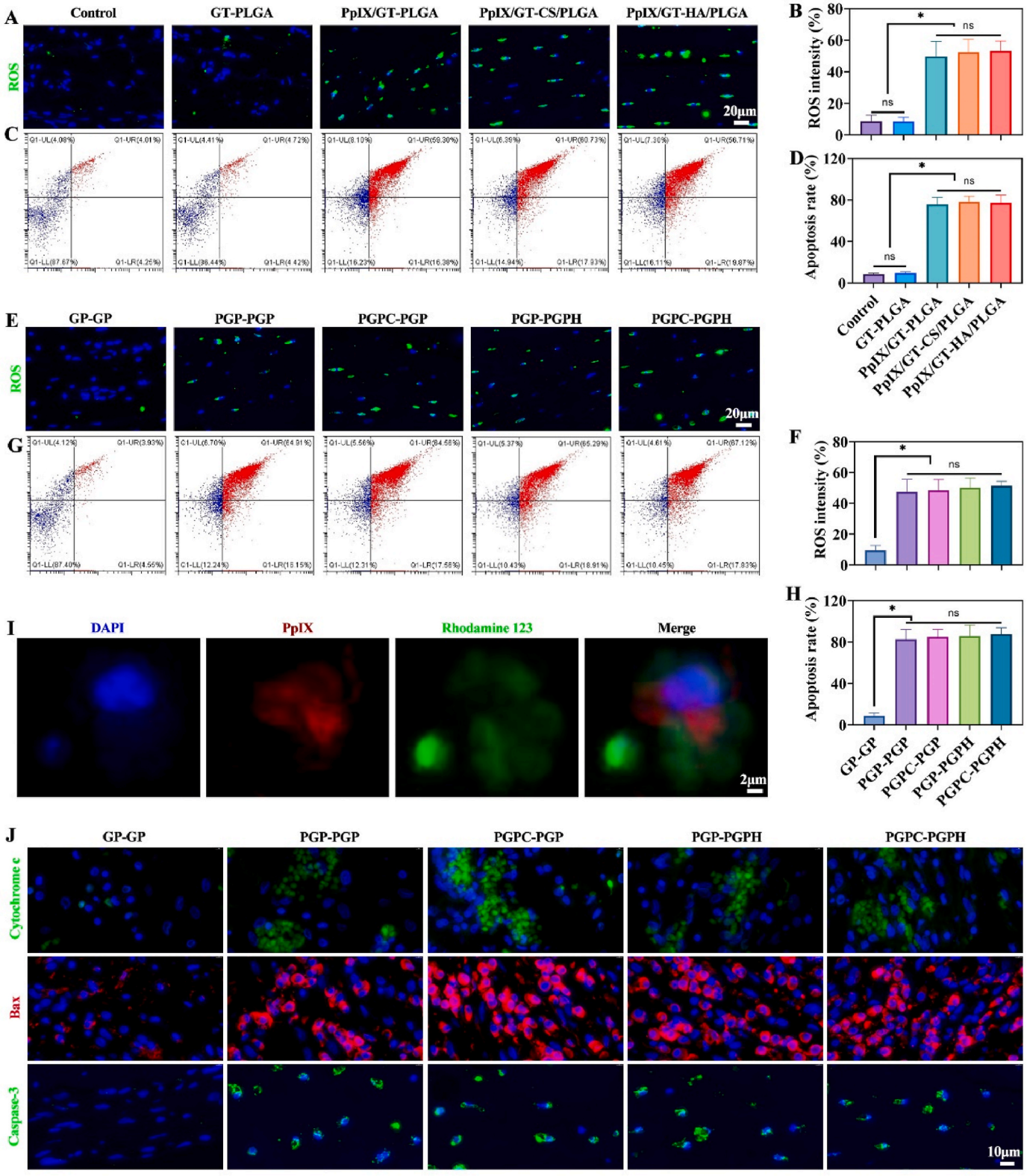


**Fig. 5.** Presents the results of apoptosis evaluations for nanofibers and 3D printed scaffolds following ultrasound irradiation of tumor cells. A) Immunofluorescence staining images of ROS and B) quantification of ROS intensity are provided for Control, GT-PLGA, PpIX/GT-PLGA, PpIX/GT-CS/PLGA, and PpIX/GT-HA/PLGA nanofibers. C) Flow cytometry detection and D) apoptosis cell rates are shown for Control, GT-PLGA, PpIX/GT-PLGA, PpIX/GT-CS/PLGA, and PpIX/GT-HA/PLGA nanofibers. E) Immunofluorescence staining images of ROS and F) quantification of ROS intensity are displayed for 3D printed GP-GP, PGP-PGP, PGPC-PGP, PGP-PGPH, and PGPC-PGPH scaffolds. G) Flow cytometry detection and H) apoptosis cell rates are presented for 3D printed GP-GP, PGP-PGP, PGPC-PGP, PGP-PGPH, and PGPC-PGPH scaffolds. I) Dual-channel imaging of PpIX and mitochondria (stained with Rhodamine 123) using an inverted CLSM in printed PGPC-PGPH scaffolds is provided. J) Immunofluorescence staining of apoptosis-related proteins (cytochrome *c*, Bax, and caspase-3) in printed GP-GP, PGP-PGP, PGPC-PGP, PGP-PGPH, and PGPC-PGPH scaffolds is shown. Significance is denoted by *, indicating $p < 0.05$, while "ns" represents no statistical significance.

to calcium influx into the mitochondria. This further induces cytochrome *c* release into the cytoplasm [31]. Cytochrome *c*, in the cytoplasm, binds with apoptotic protease-activating factor-1 (Apaf-1) to form a complex, activating caspase-9 and subsequently inducing cell apoptosis [32] (Fig. S11, Supporting Information). Additionally, the death of a small portion of GCTB cells may be due to PpIX-induced cavitation effects, which result in cell necrosis under conditions of high temperature and pressure [33].

### 3.6. In vitro osteogenic and chondrogenic differentiation of PGPC-PGPH scaffold to BMSCs

In addition to its effectiveness against GCTB cells, PGPC-PGPH scaffolds need to possess the ability to induce the osteogenic and chondrogenic differentiation of BMSCs. After co-culturing BMSCs within the printed scaffolds for 14 days, it was observed that compared to the groups without HA (control, PpIX/GT-PLGA, and PpIX/GT-CS/PLGA nanofibers, as well as printed GP-GP, PGP-PGP, and PGPC-PGP

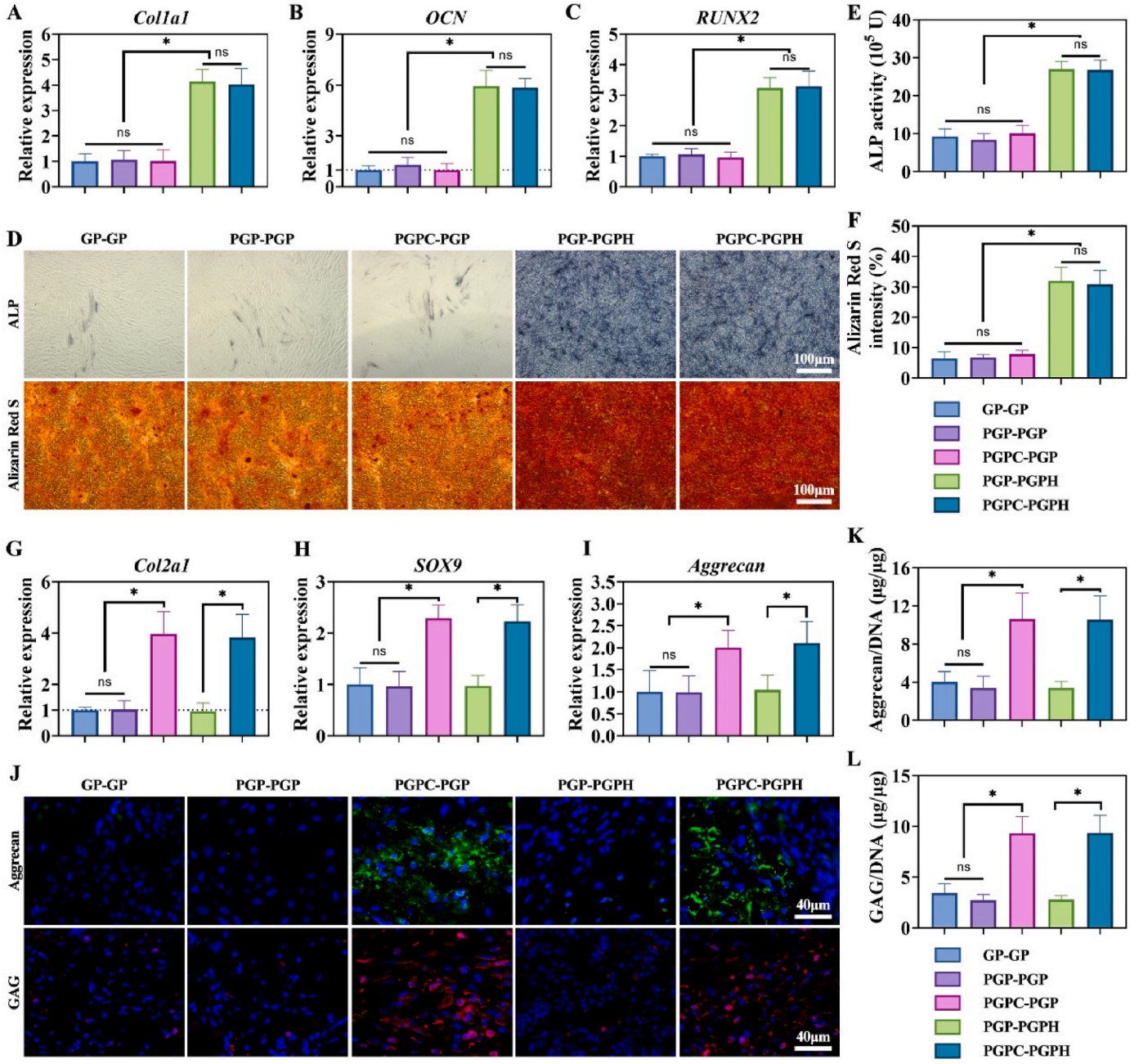


**Fig. 6.** Showcases the in vitro assessment of osteogenic and chondrogenic activities. A-C) Depict the expression levels of osteogenic-related genes (*Col1a1*, *OCN*, and *RUNX2*) via qPCR analysis in GP-GP, PGP-PGP, PGPC-PGP, PGP-PGPH, and PGPC-PGPH groups when co-cultured with BMSCs for 14 days. D) Presents ALP and Alizarin Red S staining of samples in GP-GP, PGP-PGP, PGPC-PGP, PGP-PGPH, and PGPC-PGPH groups after in vitro co-culture with BMSCs for 14 days. E-F) Provide quantitative data of ALP activity and Alizarin Red S staining intensity in GP-GP, PGP-PGP, PGPC-PGP, PGP-PGPH, and PGPC-PGPH groups following in vitro co-culture with BMSCs for 14 days. G-I) Show the expression levels of chondrogenic-related genes (*Col2a1*, *SOX9*, and *aggrecan*) via qPCR analysis in GP-GP, PGP-PGP, PGPC-PGP, PGP-PGPH, and PGPC-PGPH groups after in vitro co-culture with BMSCs for 14 days. J) Presents immunofluorescence staining of aggrecan and GAG in samples from GP-GP, PGP-PGP, PGPC-PGP, PGP-PGPH, and PGPC-PGPH groups after in vitro co-culture with BMSCs for 14 days. K-L) Offer quantitative data on aggrecan/DNA and GAG/DNA contents in GP-GP, PGP-PGP, PGPC-PGP, PGP-PGPH, and PGPC-PGPH groups after in vitro co-culture with BMSCs for 14 days. Significance is denoted by *, indicating $p < 0.05$, while "ns" represents no statistical significance.

scaffold), the HA-containing groups (PpIX/GT-HA/PLGA nanofiber, as well as printed PGP-PGPH and PGPC-PGPH scaffolds) showed significantly increased expression of osteogenic-specific genes (*Col1a1*, *OCN*, and *RUNX2*) (Fig. 6A–C and Figs. S12A–C, Supporting Information). Examination of ALP and Alizarin Red staining showed the HA-containing groups had intensive calcium salt deposition and mature osteoblast markers than the groups without HA (Fig. 6D and Fig. S12D, Supporting Information). The quantified results for ALP activity and Alizarin Red S intensity confirmed the addition of HA can effectively induce the osteogenic differentiation of BMSCs in vitro (Fig. 6E–F and Fig. S12 E-F, Supporting Information).

In contrast, compared to the groups without CS (control, PpIX/GT-PLGA, and PpIX/GT-HA/PLGA nanofibers, as well as printed GP-GP, PGP-PGP, and PGP-PGPH scaffolds), the groups containing CS (PpIX/GT-CS/PLGA nanofiber, as well as printed PGPC-PGP and PGPC-PGPH scaffolds) exhibited significantly increased expression of chondrogenic-specific genes (*Col2a1*, *SOX9*, and *aggrecan*) (Fig. 6G–I and Figs. S12G–I, Supporting Information). Immunofluorescence

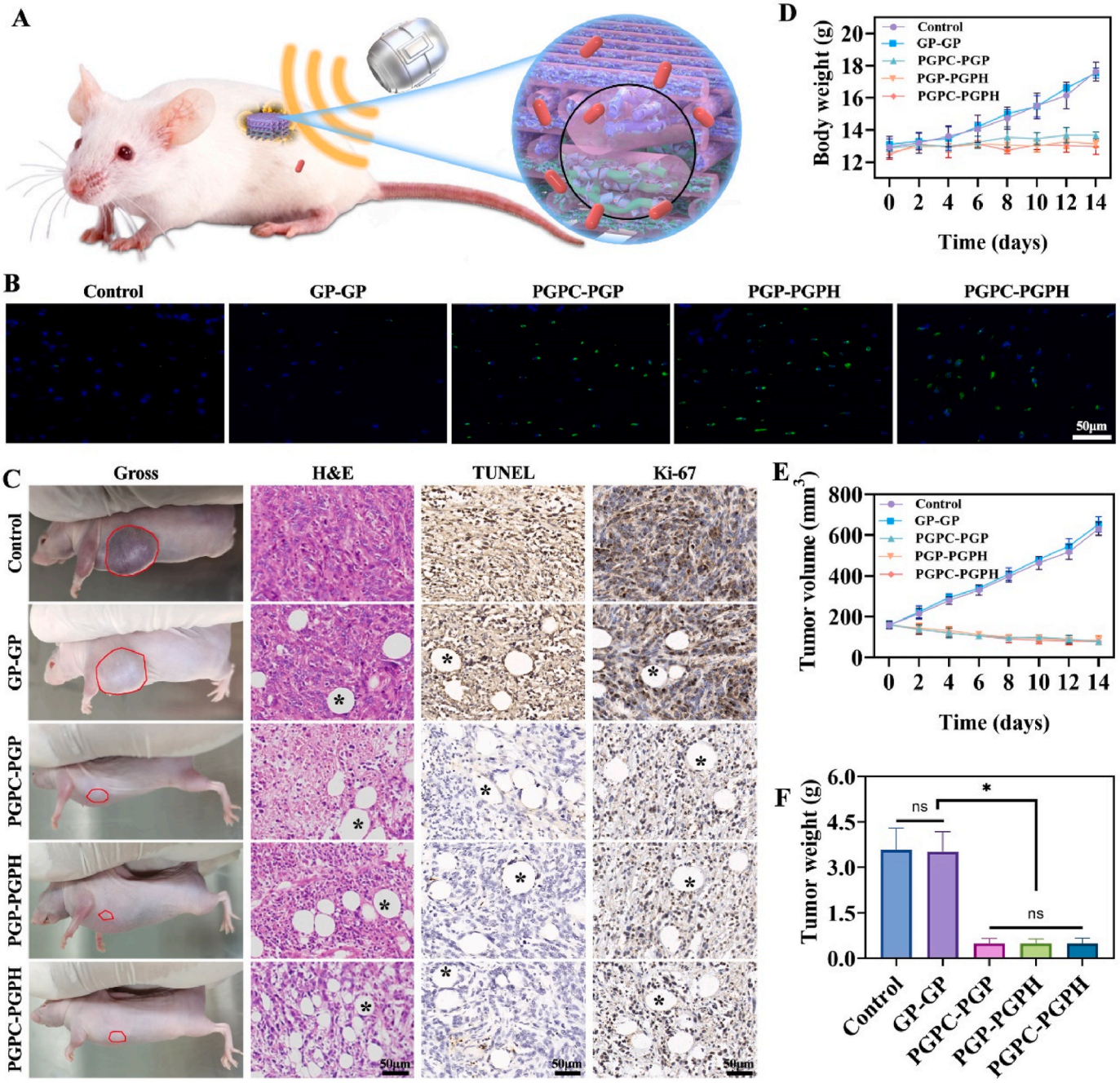


**Fig. 7.** Presents the antitumor activities in nude mice. A) A schematic illustration shows the presence of printed scaffolds within tumor-bearing nude mice upon ultrasound irradiation. B) Immunofluorescence staining for ROS in 3D printed Control, GP-GP, PGPC-PGP, PGP-PGPH, and PGPC-PGPH scaffolds immediately upon ultrasound irradiation on the 1st day. C) Offers gross observations, H&E staining, immunohistochemical TUNEL (apoptosis) and Ki-67 (proliferation) staining of samples in printed Control, GP-GP, PGPC-PGP, PGP-PGPH, and PGPC-PGPH scaffolds at 14 days post-ultrasound irradiation. D-E) Depict the changes in body weight and tumor volume of samples in printed Control, GP-GP, PGPC-PGP, PGP-PGPH, and PGPC-PGPH scaffolds from 0 to 14 days. F) Provides data on tumor weight of samples in printed Control, GP-GP, PGPC-PGP, PGP-PGPH, and PGPC-PGPH scaffolds at day 14. Significance is denoted by *, indicating $p < 0.05$, while "ns" represents no statistical significance.

staining results for aggrecan and GAG also showed significantly higher expression in the CS-containing groups compared to the groups without CS (Fig. 6J and Fig. S12J, Supporting Information). Quantitative analysis of aggrecan/DNA and GAG/DNA levels also supported the addition of CS can effectively induce the chondrogenic differentiation of BMSCs in vitro (Fig. 6K-L and Fig. S12K-L, Supporting Information).

After in vitro cultivation of BMSC-loaded printed scaffold for 21 days, immunofluorescence Col I and OCN staining demonstrated that the groups containing HA significantly promoted the osteogenic-related extracellular matrix (ECM) deposition of BMSCs compared to the groups without HA (Figs. S13A–B, Supporting Information). Safranin-O staining and immunohistochemistry COL II staining demonstrated that the CS-containing groups significantly promoted chondrogenic-related ECM secretion compared to the groups without CS (Fig. S14 A-B, Supporting Information). In summary, these data confirm that the printed double-layered PGPC-PGPH scaffold possesses the capability to induce osteogenesis in the lower layer and chondrogenesis in the upper layer, enabling "spatial control" of bone and cartilage regeneration in the correct positions.

### 3.7. In vivo antitumor effect of double-layered PGPC-PGPH scaffold upon ultrasound

This section delves into the in vivo evaluation of the printed scaffolds' effectiveness in combination with SDT against GCTB tissue in nude mice. The experiment was conducted to assess the treatment's impact on tumor tissue in vivo (Fig. 7A).

Immunofluorescence ROS labeling of tumor tissues after the first day of ultrasound treatment revealed that the non-PpIX groups (control and GP-GP scaffold) exhibited minimal ROS production. Conversely, the PpIX-containing groups (PGPC-PGP, PGP-PGPH, and PGPC-PGPH scaffolds) demonstrated intensive ROS production, highlighting the effective targeting of ROS production to the tumor site by the inclusion of PpIX in the printed scaffolds (Fig. 7B).

Gross observation of nude mice on the 14th day showed that tumors in the PpIX-containing groups were significantly smaller than those in the non-PpIX groups. Histological examinations, including H&E staining, TUNEL staining, and Ki-67 immunohistochemistry staining, revealed that the non-PpIX groups displayed intensive tumor cell proliferation and fewer apoptotic cells compared to the PpIX-containing groups (Fig. 7C). Quantification of TUNEL and Ki-67 intensity further confirmed the enhanced effectiveness of PpIX-containing groups in combating tumor cells (Figs. S15A–B, Supporting Information).

Monitoring of body weight and tumor volume changes in the mice over 14 days revealed that the body weight of mice in the PpIX groups increased over time, while the body weight of mice in the non-PpIX groups remained almost unchanged (Fig. 7D and E). In addition, the measurement of tumor weight on the 14th day indicated a clear reduction in the PpIX groups compared to the non-PpIX groups (Fig. 7F).

These results suggest that the printed scaffolds loaded with PpIX, in combination with SDT, are an extremely safe and targeted treatment method. They effectively target and affect the tumor while sparing the rest of the healthy organism, which may explain why the tumor weight decreased in the PpIX groups while the body weight of the mice remained stable. Notably, the direct implantation of scaffolds loaded with sonosensitizers into the tumor site can improve sonosensitizer accumulation and prevent their retention in healthy body parts, enhancing the precision and safety of SDT.

Considering that the in vivo experiments utilized the same GCTB cells as the in vitro experiments and the subcutaneous location of the tumor in nude mice (very close to the body surface) and SDT boasts superior penetration [8], we anticipated comparable optimal ultrasound intensity and duration both in vitro and experiments. In line with this, the in vivo experiment results of this study demonstrated that GCTB tumor-bearing nude mice treated with sonodynamic therapy (ultrasound irradiation at 2.5 MHz with PpIX) for 50 s daily remarkably achieved nearly complete regression of GCTB after a 14-day treatment period. Hence, it appears that PpIX-based sonodynamic therapy, utilizing ultrasound irradiation at 2.5 MHz with a 50-s treatment duration, holds promise as a potential treatment avenue for GCTB in clinical settings. However, it's imperative to validate the specific therapeutic effects through further clinical trials in the future.

### 3.8. In vivo evaluation of "spatial regulation" of cartilage and bone regeneration using PGPC-PGPH scaffold

This section aims to investigate the effectiveness of printed PGPC-PGPH scaffolds in spatially regulating cartilage and bone regeneration. An experimental rabbit knee OCD model was established to evaluate the regeneration capacity of these scaffolds.

After 8 weeks of postoperative recovery, the gross observation showed that the blank and GP-GP groups exhibited limited tissue repair in the defects. In contrast, the PGPC-PGP and PGP-PGPH groups displayed more substantial tissue repair. Remarkably, the PGPC-PGPH group's newly formed cartilage was nearly perfectly connected to the surrounding normal cartilage and had a very smooth surface (Fig. 8A). 3D micro-CT results further supported that the groups containing CS had relatively smoother and more newly formed cartilage surfaces, while the groups containing HA had more newly formed trabecular bone and cortical bone (Fig. 8B).

Histological examination with H&E staining, as well as toluidine blue and SO/FG staining, showed that the blank and GP-GP groups had poor regeneration of both cartilage and bone tissues in the OCD area. The PGPC-PGP and PGP-PGPH groups exhibited more moderate tissue repair. Importantly, the OCD area in the PGPC-PGPH group showed a complete filling of newly formed osteochondral tissue, with an almost perfect connection to the surrounding normal cartilage and bone (Fig. 8C and D). Results from toluidine blue and COL II immunohistochemistry staining further supported the superior cartilage formation by PGPC-PGPH scaffolds (Figs. S16A–B, Supporting Information). The immunohistochemical staining of COL I and OCN expression results showed optimal bone regeneration by PGPC-PGPH scaffolds (Fig. S17, Supporting Information).

Quantitative analyses of bone and cartilage defect repair effects, such as the ICRS and O'Driscoll histological scores, as well as bone volume fraction (BV/TV) and trabecular thickness (Tb.Th), confirmed the superior osteochondral regeneration capabilities of the double-layered PGPC-PGPH scaffold (Fig. 8E–H). Notably, the upper and lower layers of PGPC-PGPH scaffolds exhibited significant chondrogenic and osteogenic effects in their respective spatial regions, achieving precise regulation of bone and cartilage regeneration in different regions, which corresponds to "spatial regulation".

The potential clinical application of these 3D-printed scaffolds presents several acknowledged limitations and challenges: 1) This study initially demonstrated the efficacy of PC-PH scaffolds in addressing GCTB-induced osteochondral defects in different animals. Our future focus is on investigating two key sequential experiment steps within the same animal: anti-tumor mechanisms and osteochondral regeneration; 2) Further exploration and clarification of the mechanism of action of SDT is crucial to optimize its anti-GCTB function while reducing complications. 3) An upcoming challenge involves effectively enhancing ROS release efficiency and the specificity of sonosensitizer enrichment within tumor cells during SDT treatment of GCTB.

## 4. Conclusion

In our study, we developed a bilayer PGPC-PGPH porous scaffold with a shell-core structure to address two key clinical challenges in treating OCDs resulting from GCTB: the elimination of residual tumors and the promotion of OCDs regeneration. The PGPC-PGPH scaffold exhibited excellent biocompatibility and mechanical properties while effectively eradicating GCTB tissue and facilitating OCDs regeneration.

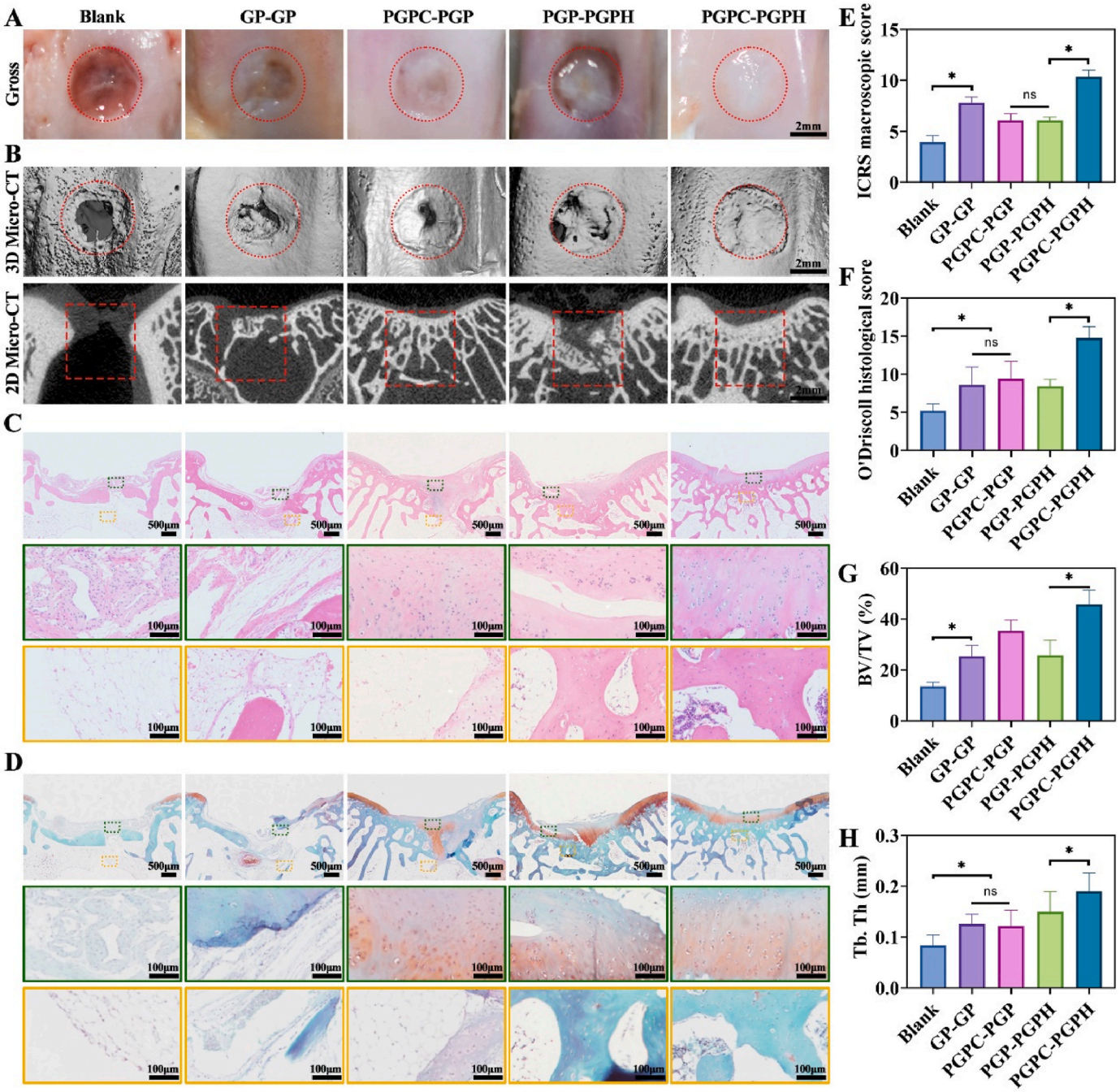


**Fig. 8.** Illustrates the osteochondral repair outcomes in rabbits at 8 weeks post-implantation. A) Provides a gross observation of the repaired tissue in the blank, GP-GP, PGPC-PGP, PGP-PGPH, and PGPC-PGPH groups. Red circles outline the osteochondral defects. B) Offers 3D reconstruction and 2D features of the repaired tissue in the blank, GP-GP, PGPC-PGP, PGP-PGPH, and PGPC-PGPH groups using Micro-CT analysis. Red circles and squares highlight the OCDs. C) Displays H&E staining of the repaired tissue in the blank, GP-GP, PGPC-PGP, PGP-PGPH, and PGPC-PGPH groups. D) Shows SO/FG staining of the repaired tissue in the same groups. Green squares indicate enlarged images in the cartilaginous zone, and yellow squares indicate enlarged images in the osseous zone. Quantitative analysis of E) ICRS score, F) O'Driscoll histological score, G) BV/TV, H) Tb.Th for the repaired tissue in the blank, GP-GP, PGPC-PGP, PGP-PGPH, and PGPC-PGPH groups. Significance is denoted by *, indicating $p < 0.05$, while "ns" represents no statistical significance.

Notably, the outer layer of the PGPC-PGPH scaffold carried sonosensitizers (PpIX) and, when exposed to extracorporeal ultrasound irradiation, selectively targeted and destroyed GCTB tissue through SDT, thus preventing tumor recurrence. The thermal effects of SDT accelerated the decomposition of the shell layer, promoting the release of CS and HA from the inner core layer. This induced the differentiation of local stem cells into cartilage and bone, precisely repairing the respective defects. The unique shell-core structure of the PGPC-PGPH scaffold allowed for temporal control, prioritizing anti-tumor treatment before tissue repair. The double-layered design enabled spatial control, ensuring precise cartilage and bone regeneration. This innovation lays the foundation for the clinical translation of "spatiotemporal-controlled" OCD treatment resulting from GCTB.

## Ethics approval and consent to participate

This study received approval from the Ethics Committee of Shanghai Pulmonary Hospital, China.

## CRediT authorship contribution statement

**Wenbao He:** Writing – original draft, Formal analysis, Data curation. **Chunlin Li:** Writing – review & editing. **Shitong Zhao:** Data curation, Investigation. **Zhendong Li:** Investigation. **Jing Wu:** Formal analysis. **Junjun Li:** Software. **Haichao Zhou:** Resources. **Yunfeng Yang:** Supervision. **Yong Xu:** Writing – review & editing, Writing – original draft, Funding acquisition. **Huitang Xia:** Funding acquisition, Conceptualization.

## Declaration of competing interest

The authors report no conflicts of interest concerning the materials or methods used in this study or the findings specified in this paper.

## Acknowledgements

This research was supported by the National Natural Science Foundation of China (82302395 and 82001979), Natural Science Foundation of Shanghai (22YF1437400), Young Elite Scientists Sponsorship Program by CAST (2023QNRC001), Shandong Provincial Natural Science Foundation (Major Basic Research Program, ZR2019ZD38), Taishan Scholar Program of Shandong Province (To Huitang Xia, 202211333), Natural Science Foundation of Shandong Province (ZR2020MH381), Academic Promotion Program of Shandong First Medical University (2019LJ005), Shandong First Medical University Culture Foundation (202201-09), and Social Science Planning and Research Project of Shandong Province (21CTQJ08).

## Appendix A. Supplementary data

Supplementary data to this article can be found online at https://doi.org/10.1016/j.bioactmat.2023.12.020.

## References

[1] A. Basu Mallick, S.P. Chawla, Giant cell tumor of bone: an update, Curr. Oncol. Rep. 23 (5) (2021) 51.
[2] A. Nagano, H. Urakawa, K. Tanaka, T. Ozaki, Current management of giant-cell tumor of bone in the denosumab era, Jpn. J. Clin. Oncol. 52 (5) (2022) 411–416.
[3] W. Liu, C.M. Chan, L. Gong, M.M. Bui, G. Han, G.D. Letson, Y. Yang, X. Niu, Malignancy in giant cell tumor of bone in the extremities, J. Bone Oncol. 26 (2021) 100334.
[4] E. Palmerini, E.L. Staals, Treatment updates on tenosynovial giant cell tumor, Curr. Opin. Oncol. 34 (4) (2022) 322–327.
[5] L. van der Heijden, A. Lipplaa, K. van Langevelde, J. Bovée, M.A.J. van de Sande, H. Gelderblom, Updated concepts in treatment of giant cell tumor of bone, Curr. Opin. Oncol. 34 (4) (2022) 371–378.
[6] H.M. Zhang, M. Guo, T.H. Zhu, H. Xiong, L.M. Zhu, A careob-like nanofibers with a sustained drug release profile for promoting skin wound repair and inhibiting hypertrophic scar, Composites Part B-Eng 236 (2022).
[7] A.Q. Zhan, L. Chen, W. Sun, Y. Tang, J. Chen, D.J. Yu, W. Zhang, Enhancement of diabetic wound healing using a core-shell nanofiber platform with sequential antibacterial, angiogenic, and collagen deposition activities, Mater. Des. 218 (2022).
[8] E.T. Ponce Ayala, F. Alves Dias de Sousa, J.D. Vollet-Filho, M. Rodrigues Garcia, L. de Boni, V. Salvador Bagnato, S. Prataviera, Photodynamic and sonodynamic therapy with protoporphyrin IX: in vitro and in vivo studies, Ultrasound Med. Biol. 47 (4) (2021) 1032–1044.
[9] Y. Xu, J. Dai, X. Zhu, R. Cao, N. Song, M. Liu, X. Liu, J. Zhu, F. Pan, L. Qin, G. Jiang, H. Wang, Y. Yang, Biomimetic trachea engineering via a modular ring strategy based on bone-marrow stem cells and atelocollagen for use in extensive tracheal reconstruction, Adv. Mater. 34 (6) (2022) e2106755.
[10] M. Chen, Y. Sun, Y. Hou, Z. Luo, M. Li, Y. Wei, M. Chen, L. Tan, K. Cai, Y. Hu, Constructions of ROS-responsive titanium-hydroxyapatite implant for mesenchymal stem cell recruitment in peri-implant space and bone formation in osteoporosis microenvironment, Bioact. Mater. 18 (2022) 56–71.
[11] H.C. Zhou, R. Chen, J.P. Wang, J. Lu, T. Yu, X.B. Wu, S.C. Xu, Z.H. Li, C. Jie, R. F. Cao, Y.F. Yang, Y.Q. Li, D.P. Meng, Biphasic fish collagen scaffold for osteochondral regeneration (vol 195, 108947, 2020), Mater. Des. 197 (2021) 1.
[12] D. Zhi, Q. Cheng, A.C. Midgley, Q. Zhang, T. Wei, Y. Li, T. Wang, T. Ma, M. Rafique, S. Xia, Y. Cao, Y. Li, J. Li, Y. Che, M. Zhu, K. Wang, D. Kong, Mechanically reinforced biotubes for arterial replacement and arteriovenous grafting inspired by architectural engineering, Sci. Adv. 8 (11) (2022) eabl3888.
[13] H. Yan, Q. Cheng, J. Si, S. Wang, Y. Wan, X. Kong, T. Wang, W. Zheng, M. Rafique, X. Li, J. He, A.C. Midgley, Y. Zhu, K. Wang, D. Kong, Functionalization of in vivo tissue-engineered living biotubes enhance patency and endothelization without the requirement of systemic anticoagulant administration, Bioact. Mater. 26 (2023) 292–305.
[14] Z. Huang, Y. Zhang, R. Liu, Y. Li, M. Rafique, A.C. Midgley, Y. Wan, H. Yan, J. Si, T. Wang, C. Chen, P. Wang, M. Shafiq, J. Li, L. Zhao, D. Kong, K. Wang, Cobalt loaded electrospun poly(epsilon-caprolactone) grafts promote antibacterial activity and vascular regeneration in a diabetic rat model, Biomaterials 291 (2022) 121901.
[15] Y. Zhang, K. Xu, D. Zhi, M. Qian, K. Liu, Q. Shuai, Z. Qin, J. Xie, K. Wang, J. Yang, Improving vascular regeneration performance of electrospun poly(ε-caprolactone) vascular grafts via synergistic functionalization with VE-cadherin/VEGF, Adv. Fiber Mater. 4 (6) (2022) 1685–1702.
[16] M. Rafique, T. Wei, Q. Sun, A.C. Midgley, Z. Huang, T. Wang, M. Shafiq, D. Zhi, J. Si, H. Yan, D. Kong, K. Wang, The effect of hypoxia-mimicking responses on improving the regeneration of artificial vascular grafts, Biomaterials 271 (2021) 120746.
[17] W. Serrano-Garcia, S. Ramakrishna, S.W. Thomas, Electrospinning technique for fabrication of coaxial nanofibers of semiconductive polymers, Polymers 14 (23) (2022).
[18] W. Chen, Y. Xu, Y. Li, L. Jia, X. Mo, G. Jiang, G. Zhou, 3D printing electrospinning fiber-reinforced decellularized extracellular matrix for cartilage regeneration, Chem. Eng. J. 382 (2020).
[19] W. Chen, Y. Xu, Y. Liu, Z. Wang, Y. Li, G. Jiang, X. Mo, G. Zhou, Three-dimensional printed electrospun fiber-based scaffold for cartilage regeneration, Mater. Des. 179 (2019).
[20] S. Al-Maawi, S. Rother, N. Halfter, K.M. Fiebig, J. Moritz, S. Moeller, M. Schnabelrauch, C.J. Kirkpatrick, R. Sader, H.P. Wiesmann, D. Scharnweber, V. Hintze, S. Ghanaati, Covalent linkage of sulfated hyaluronan to the collagen scaffold Mucograft® enhances scaffold stability and reduces proinflammatory macrophage activation in vivo, Bioact. Mater. 8 (2022) 420–434.
[21] X. Niu, N. Li, Z. Du, X. Li, Integrated gradient tissue-engineered osteochondral scaffolds: challenges, current efforts and future perspectives, Bioact. Mater. 20 (2023) 574–597.
[22] L. Yu, S. Cavelier, B. Hannon, M. Wei, Recent development in multizonal scaffolds for osteochondral regeneration, Bioact. Mater. 25 (2023) 122–159.
[23] H. Chen, X. Zhou, Y. Gao, B. Zheng, F. Tang, J. Huang, Recent progress in development of new sonosensitizers for sonodynamic cancer therapy, Drug Discov. Today 19 (4) (2014) 502–509.
[24] G. Song, H.Q. Zhao, Q. Liu, Z. Fan, A review on biodegradable biliary stents: materials and future trends, Bioact. Mater. 17 (2022) 488–495.
[25] M.C. Lee, H. Seonwoo, K.J. Jang, S. Pandey, J. Lim, S. Park, J.E. Kim, Y.H. Choung, P. Garg, J.H. Chung, Development of novel gene carrier using modified nano hydroxyapatite derived from equine bone for osteogenic differentiation of dental pulp stem cells, Bioact. Mater. 6 (9) (2021) 2742–2751.
[26] F. Yang, Y. Li, L. Wang, H. Che, X. Zhang, H. Jahr, L. Wang, D. Jiang, H. Huang, J. Wang, Full-thickness osteochondral defect repair using a biodegradable bilayered scaffold of porous zinc and chondroitin sulfate hydrogel, Bioact. Mater. 32 (2024) 400-414..
[27] F. Foglietta, P. Panzanelli, L. Serpe, R. Canaparo, Exploiting shock waves to trigger the anticancer sonodynamic activity of 5-aminolevulinc acid-derived protoporphyrin IX on in vitro 2D and 3D cancer models, Biomedicines 10 (3) (2022).
[28] L. Gao, J. Loveless, C. Shay, Y. Teng, Targeting ROS-mediated crosstalk between autophagy and apoptosis in cancer, Adv. Exp. Med. Biol. 1260 (2020) 1–12.
[29] H. Zhu, J.L. Zhou, C. Ma, D. Jiang, Y. Cao, J.J. Zhu, Self-enhanced electrochemiluminescence imaging System based on the accelerated generation of ROS under ultrasound, Anal. Chem. 95 (30) (2023) 11526–11534.
[30] S. Zaib, A. Hayyat, N. Ali, A. Gul, M. Naveed, I. Khan, Role of mitochondrial membrane potential and lactate dehydrogenase A in apoptosis, Anti Cancer Agents Med. Chem. 22 (11) (2022) 2048–2062.
[31] Y. Zhang, X. Yang, X. Ge, F. Zhang, Puerarin attenuates neurological deficits via Bcl-2/Bax/cleaved caspase-3 and Sirt3/SOD2 apoptotic pathways in subarachnoid hemorrhage mice, Biomed. Pharmacother. 109 (2019) 726–733.
[32] H. Wang, L. Zhao, J. Wu, J. Hong, S. Wang, Propofol induces ROS-mediated intrinsic apoptosis and migration in triple-negative breast cancer cells, Oncol. Lett. 20 (1) (2020) 810–816.
[33] S. Yao, Y. Zhao, Z. Wang, S. Wang, M. Zheng, Q. Hu, L. Li, Covalent organic framework nanocages with enhanced carrier utilization and cavitation effect for cancer sonodynamic therapy, ACS Appl. Mater. Interfaces 15 (29) (2023) 34488–34496.